Asymmetric photoelectron momentum distributions due to quantum interference in strong-field ionization by a few-cycle pulse

N. I. Shvetsov-Shilovski,[1] E. Räsänen,[1] G. G. Paulus,[2,3,4] and L. B. Madsen[5]

[1]*Department of Physics, Tampere University of Technology, FI-33101 Tampere, Finland*

[2]*Institute for Optics and Quantum Electronics, Friedrich-Schiller-University, Max-Wien-Platz 1, D-07743 Jena, Germany*

[3]*Helmholtz Institut Jena, Max-Wien-Platz 1, D-07743 Jena, Germany*

[4]*Department of Physics, Texas A&M University, College Station, Texas 77843, USA*

[5]*Department of Physics and Astronomy, Aarhus University, 8000 Aarhus C, Denmark*

(Received 14 January 2014; published 30 April 2014)

We calculate the left-right asymmetry of the photoelectron momentum distributions generated in a hydrogen atom exposed to an intense few-cycle laser pulse as a function of both the carrier-envelope phase and the laser intensity. We present results of the numerical solution of the three-dimensional time-dependent Schrödinger equation, semiclassical simulations accounting for both laser and Coulomb fields, and the strong-field approximation. We predict pronounced oscillations of the asymmetry parameter as a function of the intensity for a particular range of the carrier-envelope phase. In order to reveal the mechanism underlying these oscillations, we investigate in detail the electron momentum distributions in the one-dimensional case. We show that quantum interference among a large set of both bound and continuum field-free states is responsible for the oscillatory behavior of the left-right asymmetry.

DOI: 10.1103/PhysRevA.89.043431 PACS number(s): 32.80.Fb, 32.80.Rm, 32.80.Wr

I. INTRODUCTION

In strong-field physics, it has become possible to control, manipulate, and monitor electron dynamics in real time [1]. These new research directions result from remarkable developments in laser technology during the past two decades, in particular from the ability to shape and control intense near-infrared laser pulses consisting of only a few optical cycles, i.e., a few femtoseconds (see Ref. [2] for a review). The electric field of such pulses can be represented as a product of the monochromatic (carrier) wave and the envelope function. In addition to its duration, a few-cycle pulse is characterized by the phase of the carrier with respect to the maximum of the envelope, i.e., the carrier-envelope phase (CEP). Experimental evidence of the significance of the CEP was obtained in Ref. [3] for above-threshold ionization (ATI) as a violation of inversion symmetry of the photoelectron angular distribution.

The reason for the asymmetric emission of electrons liberated by a few-cycle pulse becomes particularly clear in the tunneling regime. Indeed, tunneling is a highly nonlinear process, and only a few central half cycles of the pulse contribute substantially. The heights of these relevant half cycles, and thus the ionization probabilities, depend on the CEP. In contrast to this, the CEP of a long pulse has no significant effect on photoelectron spectra due to the inversion symmetry of a monochromatic field (and of an atom).

The CEP was not controlled in the experiment of Ref. [3], but shortly thereafter remarkable progress was achieved in stabilization of the CEP (see Refs. [4–9]), and the CEP has now become a new important controllable laser parameter. A general theoretical framework for the analysis of CEP effects was presented in Ref. [10] and the case of ionization by circularly polarized light was characterized in Ref. [11]. The CEP of a few-cycle pulse affects many strong-field phenomena in atoms and molecules: high-order ATI (see Ref. [12] and references therein), high-harmonic generation (HHG) [4,13–19], nonsequential double [20–23], sequential multiple ionization [24,25], and dissociation [26]. Ionization is the initial step in these processes. Therefore, the study of the CEP effect on strong-field ionization generated by a few-cycle pulse is particularly important.

A detailed study of the asymmetry in the *low-energy part* of photoelectron spectra was carried out in Refs. [27–29]. Three different intensity regimes in which the asymmetry behaves differently were identified in Ref. [28]. They include what we refer to as the subtunneling regime between the multiphoton and tunneling regimes, with the Keldysh parameter $1 < \gamma < 2$ [30]. Here, $\gamma = \omega\kappa/F_0$ in atomic units, where ω is the carrier angular frequency, F_0 is the field strength, and $\kappa = \sqrt{2I_p}$ with I_p being the ionization potential. It was shown that in the subtunneling regime, which corresponds to the intensity range of $(0.2–1.0) \times 10^{14}$ W/cm^2 for hydrogen, the left-right asymmetry shows a stable and very simple behavior. In particular, the asymmetry depends very little on the laser intensity in this intensity range, although some oscillations were revealed. These oscillations were attributed to resonances that were Stark shifted in different ways at different intensities [28]. However, the intensity dependence of the asymmetry was investigated in Refs. [27–29] only for a few fixed values of the CEP.

The left-right asymmetry was calculated as a function of *both* the CEP and laser intensity in Ref. [31] by solving the time-dependent Schrödinger equation (TDSE) in the same subtunneling intensity range for a one-dimensional (1D) model atom. It was found that the asymmetry exhibits a nontrivial behavior: For some values of the CEP, the left-right asymmetry shows deep oscillations as a function of the laser intensity, while for others it does not, i.e., the photoelectron momentum distribution restores its symmetry at some intensities within the subtunneling region. As a result of this intricate dependency, the two-dimensional (2D) plot of the left-right ratio of the energy-integrated photoelectron yield bears resemblance to a chessboard (see Fig. 2.6. of Ref. [31] and Fig. 2 below). Furthermore, the evolution of the 2D plot of the left-right ratio with increasing pulse duration is also surprising: At some

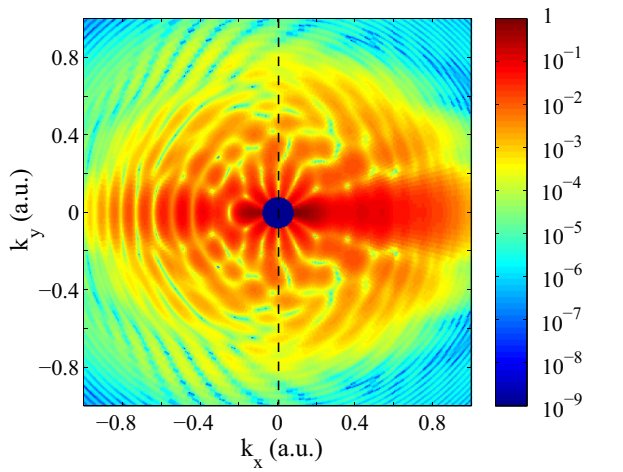

FIG. 1. (Color online) Two-dimensional photoelectron momentum distribution for $k_z = 0$ for ionization of H by a Ti:sapphire laser pulse ($\lambda = 800$ nm) with a duration of $n_p = 4$ cycles, field strength of $F_0 = 0.04$ a.u. (5.6×10^{13} W/cm^2), and CEP of $\varphi = 0.83\pi$. The Keldysh parameter is $\gamma = 1.4$. The color density is plotted in logarithmic scale.

intensities, the asymmetry parameter increases, whereas at other intensities, it decreases or even vanishes. To the best of our knowledge, the results of Ref. [31] have not been satisfactorily explained so far, and similar investigation for a real three-dimensional (3D) atom has not been carried out.

In this paper, we revisit the ionization dynamics induced by a few-cycle pulse in the subtunneling regime, in order (i) to calculate the left-right asymmetry as a function of CEP and laser intensity, (ii) to obtain deeper insight into the physical mechanism responsible for the oscillations of the asymmetry parameter, and (iii) to understand the evolution of the left-right asymmetry with increasing pulse duration. Our analysis is based on the numerical solution of the 3D TDSE, the strong-field approximation (SFA) [30,32,33], and the two-step semiclassical model [34,35]. In order to unambiguously identify the mechanism responsible for the oscillations of the asymmetry, we also consider the ionization of a 1D model atom. Indeed, the physics governing the formation of the momentum distributions will be the same as in the 3D case, and, in the 1D model, the huge computational effort associated with the continuous scan of results with both CEP and intensity is reduced to a manageable size. For the calculations in the 1D case, we use the same tools as in 3D: TDSE, 1D counterpart of the SFA, and semiclassical simulations.

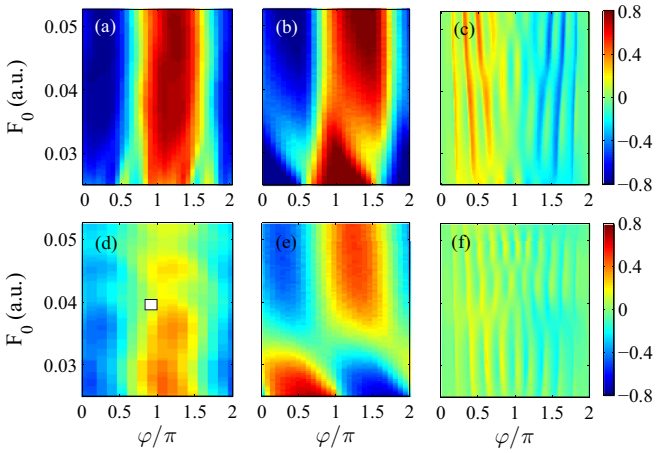

FIG. 2. (Color online) Asymmetry of the photoelectron momentum distributions as a function of the CEP and field strength for the hydrogen atom at a wavelength of 800 nm. (a),(d) The asymmetries calculated from the solution of the 3D TDSE. (b),(e) The same asymmetries calculated using the semiclassical two-step model. (c),(f) The SFA results. (a)–(c) and (d)–(f) correspond to the pulse duration $n_p = 2$ and $n_p = 4$, respectively. The point corresponding to the photoelectron momentum distribution of Fig. 1 is indicated by a white square in (d).

The paper is organized as follows. In Sec. II, we calculate and discuss the asymmetry parameter as a function of CEP and laser intensity for the real 3D atomic hydrogen. In Sec. III, we investigate the asymmetry in the 1D case, analyze the formation of the momentum distributions, and reveal the physical mechanisms underlying the intricate behavior of the left-right asymmetry. The conclusions of the paper are given in Sec. IV. Atomic units are used throughout unless indicated otherwise.

II. LEFT-RIGHT ASYMMETRY IN THREE DIMENSIONS

Before showing and discussing the results of our calculations, we briefly sketch the techniques used. Let us define a few-cycle laser pulse linearly polarized along the x axis in terms of a vector potential $\mathbf{A}(t)$:

$$\mathbf{A}(t) = (-1)^{n_p+1}\frac{F_0}{\omega}\sin^2\left(\frac{\omega t}{2n_p}\right)\sin(\omega t+\varphi)\mathbf{e}_x, \qquad (1)$$

where $\mathbf{e}_x$ is a unit vector, F_0 is the field strength, and n_p is the number of cycles within the pulse present at $t = 0 \ldots T_0$. Here, $T_0 = (2\pi/\omega)\,n_p$, where n_p is the number of cycles (here 2 or 4).

A. Time-dependent Schrödinger equation in three dimensions

For atomic hydrogen, the TDSE in the velocity gauge is given by

$$i\frac{\partial}{\partial t}\Psi(\mathbf{r},t) = \left[-\frac{1}{2}\nabla^2 - i\mathbf{A}(t)\cdot\nabla - \frac{1}{r}\right]\Psi(\mathbf{r},t), \qquad (2)$$

where the wave function is expanded in spherical harmonics,

$$\Psi(\mathbf{r},t) = \sum_{l=0}^{l_{\max}}\sum_{m=-l}^{m=l}\frac{f_{lm}(r,t)}{r}Y_{lm}(\theta,\varphi). \qquad (3)$$

A grid-based split-step method [36] is employed in the numerical procedure (see Ref. [37] for details). To find the initial state, we use the imaginary-time propagation with an equidistant radial grid consisting of 16 384 points and extending to $r_{\max} = 1000$ a.u., maximum angular momentum $l_{\max} = 40$, and a time step of 0.005 a.u. When the wave packet $\Psi(\mathbf{r},t)$ at the end of the laser pulse T_0 is known, the photoelectron momentum distribution is given by

$$\frac{\partial P}{\partial k_x \partial k_y \partial k_z} = \left|\left\langle \Psi_{\mathbf{k}}^{C-}\middle|\Psi(\mathbf{r},T_0)\right\rangle\right|^2. \qquad (4)$$

Here, $\Psi_{\mathbf{k}}^{C-}$ is a continuum scattering wave function of asymptotic momentum $\mathbf{k}$, which is obtained by solving the time-independent Schrödinger equation subject to incoming wave boundary conditions. An example of a momentum distribution obtained from a numerical solution of the TDSE is shown in Fig. 1 for $k_z = 0$. In order to be able to see the momentum distribution at higher k, we need to block out the low-energy part of the distribution. Thus we remove the low-energy part of momentum distributions $\sqrt{k_x^2 + k_y^2} < k_0$ as in Ref. [38] ($k_0 = 0.08$ a.u. in our calculations). It is clearly seen that the distribution is highly asymmetric with respect to k_x.

We define the asymmetry of the momentum distribution as

$$R = \frac{P_+ - P_-}{P_+ + P_-}. \tag{5}$$

Here, $P_- = \int_{k_x<0}(dP/dk_x dk_y)dk_x dk_y$ and $P_+ = \int_{k_x>0}(dP/dk_x dk_y)dk_x dk_y$ are the populations of the half planes $k_x < 0$ and $k_x > 0$ (both for fixed $k_z = 0$), respectively.

B. Semiclassical simulations in three dimensions

In our semiclassical approach to strong-field ionization, we follow Refs. [39,40]. Here we repeat the main points. In semiclassical simulations, the trajectory and momentum of an electron are calculated using Newton's equation of motion,

$$\frac{d^2\mathbf{r}}{dt^2} = -\mathbf{F}(t) - \frac{\mathbf{r}}{r^3}, \tag{6}$$

where $\mathbf{F}(t)$ is the electric field of the laser pulse. In order to solve Eq. (6), we need the initial velocity of the electron and the starting point of its trajectory. To obtain the latter, i.e., the tunnel exit point, we use the separation of the tunneling problem for the Coulomb potential in parabolic coordinates [41]. Note that for potentials with a non-Coulombic short-range part, this separation is approximate [42]. We also include the Stark shift of the energy level, which affects both the tunnel exit point and the ionization probability. The multielectron polarization effect (see Refs. [39,42–45]) is obviously absent for the H atom. We assume that the electron starts with zero initial velocity along the laser field $v_{||} = 0$, and nonzero initial transverse velocity $v_{0\perp}$. Both the velocity and the time of ionization t_0 are distributed according to the static ionization rate [46–48] in the tunneling regime:

$$w(t_0, v_0) \sim \exp\left(-\frac{2\kappa^3}{3F}\right)\exp\left(-\frac{\kappa v_{0\perp}^2}{F}\right), \tag{7}$$

with $F = F(t_0)$. For simplicity, we omit the preexponential factor in Eq. (7). Although this factor can affect the total ionization yield by changing it by several orders of magnitude, for atoms it only slightly affects the shape of the momentum distribution, and thus the asymmetry.

In our calculations, we use 1.5×10^6 trajectories weighted by Eq. (7). In order to solve Newton's equation of motion (6), we use a fourth-order Runge-Kutta method with adaptive step size [49]. We follow the procedure of Refs. [50,51] and exclude the trajectories that have a negative energy at the end of the laser pulse. This should be done in order to account for the possible population of Rydberg states. Furthermore, we take into account the motion of electrons with positive energies in the Coulomb field after the end of the pulse. The asymptotic momentum of an electron can be calculated from its momentum $\mathbf{q} = \mathbf{q}(t_0, v_{0\perp}, T_0)$ and position $\mathbf{r} = \mathbf{r}(t_0, v_{0\perp}, T_0)$ at the end of the laser pulse (see Refs. [39,51]),

$$\mathbf{k} = k\frac{k(\mathbf{L}\times\mathbf{a}) - \mathbf{a}}{1 + k^2L^2}, \tag{8}$$

where $\mathbf{L} = \mathbf{r}\times\mathbf{q}$ and $\mathbf{a} = \mathbf{q}\times\mathbf{L} - \mathbf{r}/r$ are the angular momentum and Runge-Lenz vector, respectively, and the absolute value of the asymptotic momentum k can be found from the energy conservation: $q^2/2 - Z/r = k^2/2$.

C. Strong-field approximation in three dimensions

In the lowest-order SFA of Ref. [30], the ionization amplitude is given by

$$M_{\mathbf{k}} = \int_0^{T_0} \langle \Psi_{\mathbf{k}}(\mathbf{r},t)|V_F(t)|\Psi_0(t)\rangle, \tag{9}$$

and the momentum distribution is obtained as the norm squared of this amplitude. In Eq. (9), $\Psi_0(t) = \Phi_0(\mathbf{r})\exp(-iE_0 t)$ is the wave function of the initial bound state, $V_F(t) = \mathbf{r}\cdot\mathbf{F}(t)$ is the interaction operator in the length gauge (see Refs. [32,33] for velocity gauge versions of the SFA), and

$$\Psi_{\mathbf{k}}(\mathbf{r},t) = \frac{1}{(2\pi)^{3/2}}\exp\left\{i[\mathbf{k} + \mathbf{A}(t)]\cdot\mathbf{r} - \frac{i}{2}\int^t [\mathbf{k} + \mathbf{A}(t')]^2 dt'\right\} \tag{10}$$

is the Volkov wave function in the same gauge normalized such that $\langle\Psi_{\mathbf{k}}(\mathbf{r},t)|\Psi_{\mathbf{k}'}(\mathbf{r},t)\rangle = \delta(\mathbf{k} - \mathbf{k}')$. After some transformations using the Schrödinger equation (see Refs. [52,53] for details), the amplitude can be rewritten as

$$M_{\mathbf{k}} = \int_0^{T_0}\left\{E_0 - \frac{1}{2}[\mathbf{k} + \mathbf{A}(t)]^2\right\}\tilde{\Phi}(\mathbf{k} + \mathbf{A}(t)) \times \exp[if(t)]dt, \tag{11}$$

where

$$\tilde{\Phi}(\mathbf{q}) = \int e^{-i\mathbf{q}\cdot\mathbf{r}}\Phi_0(\mathbf{r})d\mathbf{r} \tag{12}$$

is the Fourier transform of $\Phi_0(\mathbf{r})$, and

$$f(t) = \frac{1}{2}\int^t [\mathbf{k} + \mathbf{A}(t')]dt' - E_0 t \tag{13}$$

is a rapidly oscillating function. This rapidly oscillating phase implies that the amplitude of Eq. (11) can be evaluated accurately using the saddle-point method. The saddle-point equation reads

$$[\mathbf{k} + \mathbf{A}(t)]^2 + \kappa^2 = 0. \tag{14}$$

For the ground ($1s$) state of hydrogen, $\Phi_0(\mathbf{r}) = (2/\sqrt{4\pi})\exp(-r)$, and, therefore, $\tilde{\Phi}(\mathbf{q}) = 4\sqrt{4\pi}/(1 + q^2)^2$. Substituting this expression into Eq. (11) and taking into account that $E_0 = -0.5$ a.u., we obtain

$$M_{\mathbf{k}} = -2\sqrt{4\pi}\int_0^{T_0}\frac{\exp[if(t)]}{[\mathbf{k} + \mathbf{A}(t)]^2 + \kappa^2}dt. \tag{15}$$

The integrand of Eq. (15) is singular at the saddle points, so that the method has to be modified (see Ref. [52] for details). The modified saddle-point solution for the integral (15) reads

$$M_{\mathbf{k}} = \sum_{t_S} \frac{2\pi^{3/2} i}{f''(t_S)} \exp[i f(t_S)], \tag{16}$$

where the summation is carried out over all the saddle points t_S corresponding to a given final momentum $\mathbf{k}$. The saddle points are found with the Newton-Raphson method [49] in the complex plane. As in Ref. [53], the initial approximation for the solution of Eq. (14) is found by considering the behavior of $|f(t)|^{-1/2}$ for each momentum $\mathbf{k}$.

D. Left-right asymmetry

The left-right asymmetry parameter R [Eq. (5)] calculated for hydrogen over the range of intensities is shown in Fig. 2 for two different pulse durations as a function of the CEP. The first column of Fig. 2 shows the results of the numerical solution of the TDSE, whereas the second and the third columns correspond to the results of the semiclassical simulations and the SFA, respectively. We remind the reader that in this paper we focus on the subtunneling regime with field strengths $0.025 < F_0 < 0.055$ a.u.

First we turn our attention to Figs. 2(a) and 2(d). In the low-intensity part, where $F_0 \lesssim 0.03$ a.u., the asymmetry parameter demonstrates irregular behavior as a function of the CEP for both $n_p = 2$ and $n_p = 4$. For H, the fields $F_0 < 0.03$ a.u. correspond to $\gamma > 1.9$, i.e., the multiphoton regime. In the multiphoton regime, lowest-order perturbation theory has been used to analyze the origin of the left-right asymmetry [54,55]. The criterion for the applicability of the two-step model developed in Ref. [40] shows that the semiclassical model is not valid in this intensity range. This inapplicability manifests itself in the change of the behavior of R around $F_0 = 0.03$ a.u. [compare Figs. 2(e) and 2(b)].

It is seen in Fig. 2(d) that for $n_p = 4$, the asymmetry shows clear oscillations as a function of the laser intensity for a fixed CEP. Note that the semiclassical simulations, even accounting for the Coulomb potential, cannot describe these oscillations of the asymmetry; see Fig. 2(c). It is interesting to note that the two-step model accounting for both laser and Coulomb fields shows a good quantitative agreement with the TDSE result when describing the dependence of the left-right asymmetry on the CEP for some fixed laser intensities; see Ref. [29]. This shows that some physical mechanism other than the Coulomb attraction of the continuum electron to the ion is responsible for the change of the symmetry of momentum distributions and, therefore, for the oscillations of R. Finally, and in accord with Refs. [28,29], the SFA is also inapplicable for the description of the asymmetry [see Figs. 2(c) and 2(f)] of momentum distributions in the low-energy part of the ATI spectrum. However, this is not the case for high-order ATI. The SFA amplitude accounting for the rescattering term describes the left-right asymmetry of the photoelectron spectrum well enough, provided the asymmetry is defined only for high-energy plateau of the spectrum but not for its low-energy part.

III. ANALYSIS OF THE LEFT-RIGHT ASYMMETRY IN A ONE-DIMENSIONAL MODEL

The momentum distributions are numerically much faster to calculate in a 1D model than in the 3D case, and the analysis of the origin of the asymmetry is also simpler (see below). For our analysis, we apply the same methods as in the 3D case in Sec. II: direct numerical solution of the TDSE, semiclassical simulations, and 1D counterpart of the SFA. As in Sec. II, let us first discuss these methods in more detail.

A. One-dimensional time-dependent Schrödinger equation in coordinate space

In the length gauge, the 1D TDSE for an electron in the laser pulse reads

$$i\frac{\partial}{\partial t}\Psi(x,t) = \left\{ -\frac{1}{2}\frac{\partial^2}{\partial x^2} + V(x) + F(t)x \right\}\Psi(x,t). \tag{17}$$

Here, $V(x)$ is a binding potential and $F(t)$ is the laser field. As the binding potential, we use the soft-core Coulomb potential,

$$V(x) = -\frac{Z}{\sqrt{x^2 + a^2}}, \tag{18}$$

with $a = 1.0$ and $Z = 1.0$ as in, e.g., Ref. [56]. These parameter values are used throughout the paper. We mention, however, that with values $a = 1.0$ and $Z \approx 0.7795$ the ground-state energy becomes $E_0 = -0.50$ a.u. as in real (3D) hydrogen atom.

In order to solve Eq. (17), we follow the approach of Refs. [56,57], where the TDSE is solved on a grid, and derivatives are approximated by finite differences. We use a 1D box centered at $x = 0$ and extending to $\pm X_{\max}$. For the time propagation, we use a standard Cranck-Nicholson scheme (see, e.g., Ref. [49]). Although we impose zero boundary conditions at $x = \pm X_{\max}$, we do not allow the wave packet to approach the boundary by using a sufficiently large box size. As in the 3D case, the smaller grid spacing requires a smaller time step for a stable solution. Typically, our grid consists of 128 000 points and extends up to $X_{\max} = 4000$ a.u., and the time step is $\Delta t = 7 \times 10^{-4}$ a.u. The most straightforward way to calculate 1D momentum distributions can be expressed as follows (see Ref. [58]):

$$\frac{dP}{dk_x} = \lim_{t\to\infty} |\langle \Psi_{k_x}(x)|\hat{P}_C \Psi(x, T_0 + t)\rangle|^2. \tag{19}$$

Here, $\Psi_{k_x}(x) = \exp(ik_x x)/\sqrt{2\pi}$ is a plane wave with momentum k_x, and $\hat{P}_C = 1 - \sum_n |\Psi_n\rangle\langle\Psi_n|$, where the sum is taken over all the bound states. In practice, $t = 3T_0$ is enough to get a stabilization of the momentum distribution with an uncertainty of less than 1%. The left-right ratio P_+/P_- is in agreement with Fig. 2.6 in Ref. [31], when it is calculated for the same few-cycle pulse defined via its electric field with the Gaussian envelope

$$F(t) = F_0 \exp\left(-\frac{2\ln 2}{\tau^2} t^2 \right) \cos(\omega t + \varphi), \tag{20}$$

and for same binding potential, $V(x) = -0.7795/\sqrt{x^2 + a_0^2}$.

B. Semiclassical simulations in one dimension

The semiclassical simulations in 1D are performed similarly to the 3D case. Newton's equation of motion now reads

$$\frac{d^2x}{dt^2} = -F(t) - \frac{dV(x)}{dx}. \tag{21}$$

As in the 3D case, we assume that the electron has zero initial velocity in the direction of the laser field, $\dot{x}(t_0) = 0$. The tunnel exit point $x(t_0)$ is found from the following equation:

$$V(x) + F(t)x = E_0. \tag{22}$$

The time of the ionization is again distributed in accord with the static tunneling rate,

$$w(t_0) \sim \exp\left(-\frac{2\kappa_0^3}{3F}\right), \tag{23}$$

with $F = F(t_0)$ and $\kappa_0^2/2 = E_0$. In contrast to the 3D case, we need fewer ($\sim 1.0 \times 10^5$) trajectories to resolve 1D momentum distributions because there is no sampling over the transverse initial momenta. We propagate the ensemble of trajectories after the end of the laser pulse until the electron momentum distribution converges. Typically, 8–10 laser periods are enough.

C. Strong-field approximation in one dimension

We introduce the SFA in 1D similarly to the 3D case [cf. Eq. (9)]:

$$M_{k_x} = \int_0^{T_0} \langle \Psi_{k_x}(x,t)|V_F(t)|\Psi_0(x,t)\rangle, \tag{24}$$

where $\Psi_0(x,t) = \phi_0(x)\exp(-iE_0t)$ is the initial wave function, $V_F(t) = xF(t)$ is the interaction operator, and

$$\Psi_{k_x}(x,t) = \frac{1}{(2\pi)^{1/2}}\exp\left\{i[k_x + A_x(t)]x - \frac{i}{2}\int^t [k_x + A_x(t')]^2 dt'\right\} \tag{25}$$

is the 1D analog of the Volkov state, normalized such that $\langle \Psi_{k_x}(x,t)|\Psi_{k_x'}(x,t)\rangle = \delta(k_x - k_x')$. The same transformations as in the 3D case lead to the following expression for the ionization amplitude:

$$M_{k_x} = \int_0^{T_0}\left\{E_0 - \frac{1}{2}[k_x + A_x(t)]^2\right\}\tilde{\phi}_0[k_x + A_x(t)] \times \exp[if(t)]dt, \tag{26}$$

where

$$\tilde{\phi}_0(q) = \int e^{-iqx}\phi_0(x)dx \tag{27}$$

is the Fourier transform of the initial bound state $\phi_0(x)$, and

$$f(t) = \frac{1}{2}\int^t [k_x + A_x(t')]^2 dt' - E_0 t. \tag{28}$$

The saddle-point equation in 1D reads similar to the 3D case; see Eq. (14). It is easy to verify that the Fourier transform of Eq. (27) is again singular at the saddle points. However, and in contrast to the 3D case, we do not have any analytic expression for the initial bound state $\phi_0(x)$. Therefore, we calculate the integral in Eq. (26) numerically. Since the integrand is a highly oscillating function, the standard methods of numerical integration are inefficient. Thus, it is reasonable to use a numerical method specially adapted to the evaluation of highly oscillating integrals. Let us first rewrite Eq. (26) as follows:

$$M_{k_x} = \frac{1}{\omega}\int_0^{\omega T_0} F(\omega t)\exp[iz_F\xi(\omega t)]d(\omega t), \tag{29}$$

where

$$F(\omega t) = \left\{\frac{1}{2}[k_x + A_x(t)]^2\right\}\tilde{\phi}_0(k_x + A_x(t)), \tag{30}$$

$\xi(\omega t) = f(t)/z_F$, and $z_F = F^2/\omega^3 \gg 1$. Following the approach of Refs. [59,60], we use the transformation $x = \xi(\omega t)$ to yield an integral of the form

$$M_{k_x} = \frac{1}{\omega}\int_0^{\omega T_0} \frac{F[\xi^{-1}(x)]}{\xi'[\xi^{-1}(x)]}\exp[iz_F x]dx. \tag{31}$$

Since the saddle-point equation for integral (26) does not have real solutions, $\xi'(\omega t)$ has no zeros on the interval of integration, and the integral of Eq. (31) is nonsingular. This integral can be easily calculated using Filon's integration formula [61]. It should be stressed that the same integration technique can also be applied to calculate the usual SFA ionization amplitude in 3D. The numerical calculation of the highly oscillating integral in Eq. (11) takes only a few minutes on a single 2.7 GHz processor.

D. Asymmetry in one dimension

The asymmetry parameters calculated for the 1D model atom with the binding potential of Eq. (18) with $Z = 1$ and with same pulse durations as in Fig. 2 are shown in Fig. 3.

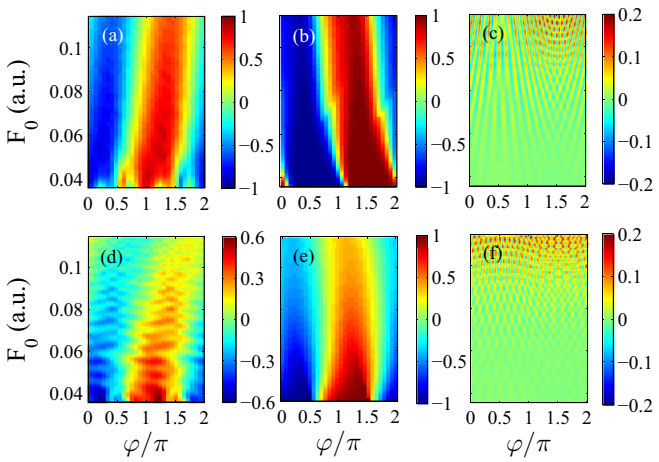

FIG. 3. (Color online) Asymmetry of the photoelectron momentum distributions as a function of the CEP and field strength for a 1D model atom with soft-core potential given by Eq. (18) and for a wavelength of 800 nm. (a)–(c) and (d)–(f) correspond to the pulse durations $n_p = 2$ and $n_p = 4$, respectively. (a) and (d) show the asymmetries calculated from the solution of the 1D TDSE. (b) and (e) present the asymmetries calculated using the two-step model. (c) and (f) depict the results of the 1D SFA.

Note that in the 1D case, the asymmetry oscillations are very sensitive to both the envelope of the laser pulse and the binding potential. As in the 3D case, the two-step model in the combined ionic potential and the electric field of the pulse is not capable to describe the intensity dependence of the asymmetry parameter; see Figs. 3(b) and 3(e). The same is true for the SFA, which (i) predicts qualitatively different behavior of the asymmetry as a function of laser intensity and CEP, and (ii) substantially underestimates the asymmetry of the distributions [see Figs. 3(c) and 3(f)]. However, Fig. 3 does not give much insight into the *mechanism* underlying the complex behavior of the asymmetry as one could expect.

In view of the failure of the two-step model and the SFA, it appears reasonable to expect that the participation of atomic resonances in the ionization dynamics is responsible for the intricate oscillations of the asymmetry. Indeed, this hypothesis might explain the behavior of R with a decrease of the pulse duration, as well as its sensitivity to the parameters of the potential and to the envelope function. In order to investigate this suggestion, we monitor the populations of the ground state and of the few first excited states during the laser pulse for a fixed CEP with $\varphi = 0$ and several different field amplitudes, for which the asymmetry R has different signs. Surprisingly, it is found that the populations do not exhibit any notable resonancelike behavior.

1. Role of the continuum

In order to shed light on the oscillations of R, in Figs. 4(a) and 4(b) we plot the ionized part of the momentum-space wave function during the laser pulse for a fixed CEP with $\varphi = 0.83\pi$ and for two different field amplitudes $F_0 = 0.076$ a.u. and 0.079 a.u. corresponding to asymmetries $R = -0.04$ and $R = 0.02$, respectively. The corresponding momentum distributions at the end of the pulse ($t = T_0$) are shown in Figs. 4(c) and 4(d). Note that these distributions are similar to those at $t \to \infty$: The calculations show that there is no substantial exchange of the population between the $k_x < 0$ and $k_x > 0$ semiaxes after the laser field is switched off. It is seen in Figs. 4(c) and 4(d) that the momentum distribution dP/dk_x is nonzero at approximately the same interval $\Delta k \approx 2.0$ a.u. for both $k_x < 0$ and $k_x > 0$. Thus the sign of the asymmetry is determined by the position of the maximum of the distribution [cf. Figs. 4(c) and 4(d)].

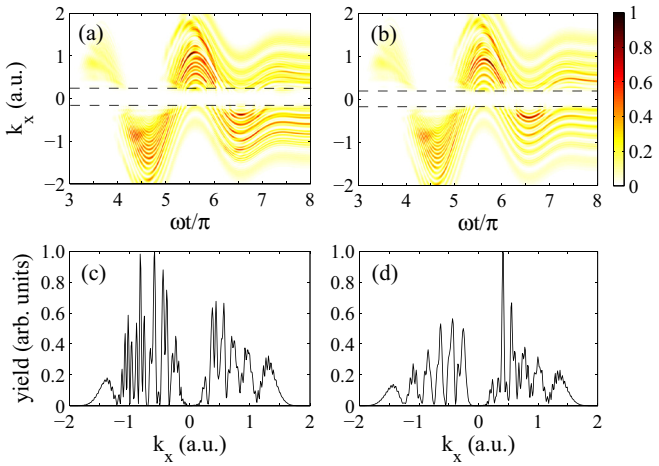

FIG. 4. (Color online) (a),(b) Ionized part of the wave function in momentum space during the laser pulse defined by the vector potential (1) for 1D model atom [Eq. (18)], and (c),(d) momentum distributions at the end of the pulse in Eq. (1). The areas contained within the dashed lines in panels (a) and (b) correspond to the bound-state part of the wave packet. Panels (a) and (c) correspond to $F_0 = 0.076$ a.u., whereas (b) and (d) show results for $F_0 = 0.079$ a.u. The wavelength is $\lambda = 800$ nm, the pulse duration is $n_p = 4$, and the CEP is $\varphi = 0.83\pi$.

In order to analyze the effect in more detail, we turn to the TDSE in the momentum space and velocity gauge,

$$i\frac{\partial\tilde{\phi}(k_x,t)}{\partial t} = \frac{k_x^2}{2}\tilde{\phi}(k_x,t) + k_x A_x(t)\tilde{\phi}(k_x,t) + \int_{-\infty}^{\infty} V(k_x,k_x')\tilde{\phi}(k_x',t)dk_x', \quad (32)$$

where $\tilde{\phi}(k_x,t)$ is the momentum-space wave function, and

$$V(k_x,k_x') = \frac{1}{\sqrt{2\pi}}\int V(x)\exp[i(k_x - k_x')]dx \quad (33)$$

is the kernel of integral-differential equation (32). For brevity, we omit infinite integration limits in Eq. (33) and in the following. The corresponding time-independent equation in the absence of the laser field reads

$$\frac{k_x^2}{2}\tilde{\phi}(k_x) + \int V(k_x,k_x')\tilde{\phi}(k_x')dk_x' = E\tilde{\phi}(k_x). \quad (34)$$

Since the eigenstates $\tilde{\phi}_m(k_x)$ of the field-free Hamiltonian form a complete set, the wave function $\tilde{\phi}(k_x,t)$ at any time t can be written as

$$\tilde{\phi}(k_x,t) = \sum_m c_m(t)\tilde{\phi}_m(k_x)\exp(-iE_m t), \quad (35)$$

where E_m is an eigenvalue corresponding to the eigenvector $\tilde{\phi}_m(k_x)$. Note that the coefficients c_m of the expansion of Eq. (35) are generally complex. By inserting Eq. (35) into Eq. (32), taking into account Eq. (34), and integrating over k_x, we obtain

$$i\frac{dc_n}{dt} = \sum_m c_m(t)F_{nm}A_x(t)\exp[-i(E_m - E_n)t]. \quad (36)$$

Here, F_{nm} is a matrix element of momentum operator $\hat{k}_x$ between the states m and n:

$$F_{nm} = \int \tilde{\phi}_n(k_x)k_x\tilde{\phi}_m(k_x)dk_x. \quad (37)$$

Note that since we impose zero boundary conditions, the eigenfunctions $\tilde{\phi}_n(x)$ are real and, therefore, $\tilde{\phi}_n^*(k_x) \equiv \tilde{\phi}_n(k_x)$.

In order to solve Eq. (34), we use a 1D box centered at $k_x = 0$ and extending to $K_{\max} = 10$ a.u. The grid in momentum space consists of 5000 points. The basis we use in the expansion [Eq. (35)] consists of 1500 eigenstates, in which 50 correspond to bound states and the rest form a discretized continuum.

The solution of Eq. (36), i.e., the set of complex coefficients $c_m(t)$, yields the wave function in Eq. (35). From the computational point of view, Eq. (37) does not give any advantages compared to the direct solution of the TDSE

either in coordinate or momentum space. First, to achieve convergence, we need to have a large number of basis functions in the expansion of Eq. (35), typically $m = 1000$–1500. Second, owing to the large number of equations needed, Eq. (37) demonstrates rather unstable behavior for some laser-atom parameters. In order to solve Eq. (37), we used the implicit (backward) Euler method (see, e.g., [49]) instead of the conventional Runge-Kutta method with an adaptive step-size control. However, the implicit Euler method requires the solution of a system of linear algebraic equations at each time step, and the matrix of this system is neither tridiagonal nor sparse.

Let us denote the phase of the coefficient $c_m(t)$ by α_m, i.e., $c_m(t) \equiv |c_m(t)| \exp(i\alpha_m)$. Now, Eq. (35) can be rewritten as

$$\tilde{\phi}(k_x,t) = \sum_{m=m_0} |c_m(t)| \tilde{\phi}_m(k_x) \exp(i\beta_m), \tag{38}$$

where $\beta_m = \alpha_m - E_m t$. Numerical solution of Eq. (36) shows that for the parameters of Fig. 3, the contributions of almost all continuum states to the sum of Eq. (43) are of the same order of magnitude, and only terms with $m \gtrsim 1000$ can be neglected. Note that the summation in Eq. (38) starts from some m_0, which corresponds to the first positive eigenvalue $E_{m_0} > 0$ ($m_0 = 51$ for $K_{\max}$ and number of grid points we used). In order to obtain the momentum distribution, we have to calculate $|\tilde{\phi}(k_x,t)|^2$ at $t \to \infty$:

$$\begin{aligned} |\tilde{\phi}(k_x,t)|^2 = & \sum_{m=m_0} |c_m(t)|^2 \tilde{\phi}_m^2(k_x) \\ & + \sum_{\substack{m=m_0 \\ n>m}} 2|c_m(t)||c_n(t)| \tilde{\phi}_m(k_x)\tilde{\phi}_n(k_x) \\ & \times \cos(\beta_m - \beta_n). \end{aligned} \tag{39}$$

It is obvious that not all of the terms in Eq. (39) will contribute to the asymmetry of the distribution. Although $\tilde{\phi}_m(k_x)$ is an even function for odd m, and an odd function for even m, $|\tilde{\phi}(k_x)|^2$ (as well as $|\tilde{\phi}(k_x)|$) is an even (symmetric) function for any m. Therefore, only some of the interference terms [i.e., some terms of the second sum on the right side of Eq. (39)] are asymmetric, provided that $\tilde{\phi}_m(k_x)\tilde{\phi}_n(k_x)$ is an odd function. This, in turn, implies that $\tilde{\phi}_m(k_x)$ is an odd function, and $\tilde{\phi}_n(k_x)$ is an even function, or vice versa. For an odd function $\tilde{\phi}_m(k_x)\tilde{\phi}_n(k_x)$, the integrals $\int_{k_x<0} \tilde{\phi}_m(k_x)\tilde{\phi}_n(k_x)\,dk_x$ and $\int_{k_x>0} \tilde{\phi}_m(k_x)\tilde{\phi}_n(k_x)\,dk_x$ have the same absolute values but different signs. As a result, asymmetric contributions to both $\int_{k_x<0} |\tilde{\phi}(k_x,t\to\infty)|^2 dk_x$ and $\int_{k_x>0} |\tilde{\phi}(k_x,t\to\infty)|^2 dk_x$ have different signs but equal absolute values. The analysis presented here provides decisive evidence that quantum interference is responsible for the left-right asymmetry.

Below we derive a formula, which allows one to calculate the sign of the asymmetry, provided the solution of the TDSE given by Eq. (36) is known. Let us denote $P_+ \equiv S_0 + \Delta$ and $P_- \equiv S_0 - \Delta$, where S_0 is an equal, i.e., symmetric contribution to the areas under the curve $|\tilde{\phi}(k_x,t\to\infty)|^2$ for both $k_x < 0$, and $k_x > 0$. Then the asymmetry is calculated as

$$R = \frac{\Delta}{S_0}, \tag{40}$$

and, therefore, the sign of R is determined from the sign of

$$\Delta = \sum_{\substack{m=m_0 \\ n>m}} 2|c_m(t)||c_n(t)| \cos(\beta_n - \beta_m) \int_{k_x>0} \tilde{\phi}_m(k_x)\tilde{\phi}_n(k_x)dk_x. \tag{41}$$

Note that for each n in Eq. (41), we should consider $n = m+1, m+3, m+5, \ldots$. Furthermore,

$$\begin{aligned} \left| \int_{k_x>0} \tilde{\phi}_m(k_x)\tilde{\phi}_{m+1}(k_x)dk_x \right| &> \left| \int_{k_x>0} \tilde{\phi}_m(k_x)\tilde{\phi}_{m+3}(k_x)dk_x \right| \\ &> \left| \int_{k_x>0} \tilde{\phi}_m(k_x)\tilde{\phi}_{m+5}(k_x)dk_x \right| > \cdots, \end{aligned} \tag{42}$$

since $\tilde{\phi}_{m+k}(k_x)$ "moves away" from $\tilde{\phi}_m(k_x)$ with increasing k, and their overlap decreases. Therefore, the main contribution to the asymmetry for fixed m is given by the interference term proportional to $\tilde{\phi}_m(k_x)\tilde{\phi}_{m+1}(k_x)$. For example, $\int_{k_x<0} \tilde{\phi}_{51}(k_x)\tilde{\phi}_{52}(k_x)dk_x \approx -0.5000$, $\int_{k_x<0} \tilde{\phi}_{51}(k_x)\tilde{\phi}_{54}(k_x)dk_x \approx 0.0057$, $\int_{k_x<0} \tilde{\phi}_{51}(k_x)\tilde{\phi}_{56}(k_x)dk_x \approx -0.0029$, etc. Therefore, the main contribution to the asymmetry for fixed m is given by the term proportional to $\tilde{\phi}_m(k_x)\tilde{\phi}_{m+1}(k_x)$. This allows us to estimate the asymmetric contribution to the population $\int_{k_x>0} |\tilde{\phi}(k_x,t\to\infty)|^2 dk_x$ as

$$\Delta \approx \sum_m 2\Gamma_m |c_m(t)||c_{m+1}(t)| \cos(\beta_m - \beta_{m+1}), \tag{43}$$

where $\Gamma_m = \int_{k_x>0} \tilde{\phi}_m(k_x)\tilde{\phi}_{m+1}(k_x)dk_x$, provided that $|c_m(T_0)||c_{m+1}(T_0)| \gtrsim |c_m(T_0)||c_{m+3}(T_0)| \gtrsim |c_m(T_0)||c_{m+5}(T_0)| \gtrsim \cdots$, which is true for the parameters used in Fig. 3 [note that according to Eq. (36), the coefficients $c_m(t)$ are constant at $t \geqslant T_0$]. Note that Eq. (43) does not have any predictive power: in order to obtain the sign of the asymmetry, one has to solve TDSE first. However, Eq. (43) can be used to calculate the sign of the asymmetry parameter R if the coefficients $c_m(t)$ are known. For example, for $F_0 = 0.076$ a.u. and 0.079 a.u. (and for a fixed CEP of $\varphi = 0$), the estimate of Eq. (43) gives $\Delta = -3 \times 10^{-4}$ and $\Delta = 3 \times 10^3$, respectively, and thus reproduces the correct signs of R. Note that the statements in the above analysis about the overlaps between field-free basis states do not depend on the laser parameters; only the expansion amplitudes $c_n(t)$ do.

2. *Role of the bound states*

The analysis presented above is insufficient to understand the role of the bound states in the formation of the asymmetry. Indeed, is there interference of only the continuum channels or is the asymmetry induced by the bound part of the wave packet that is carried into the continuum during the laser pulse? In order to answer this question, we next consider the solution of the TDSE with all of the continuum states and only *some* of the bound states included in the expansion of Eq. (35). The asymmetry as a function of the CEP and laser intensity is shown in Fig. 5 for different number of bound states taken into account. This figure should be compared with Figs. 3(d)–3(f). As one could expect, the low-intensity part of Fig. 5(a) (with only the ground state) is similar to the result of the two-step model [cf. Fig. 3(e)], whereas its high-intensity part slightly resembles the SFA result [cf. Fig. 3(f)]. In the sequence of

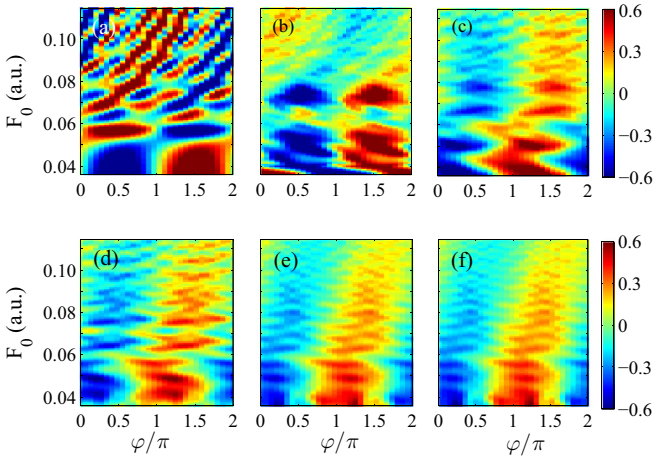

FIG. 5. (Color online) Asymmetry of the photoelectron momentum distributions as a function of the CEP and field strength for a 1D model atom with soft-core potential given by Eq. (18) at a wavelength of 800 nm and for $n_p = 4$. (a) The asymmetry when only the ground state is included. (b) The case when the ground state and first excited state are taken into account. (c) The asymmetry when the ground state and the first through fourth excited states are included. (d)–(f) The inclusion of the ground state and all the excited states up to the 10th, 20th, and 30th state, respectively. In all cases (a)–(f), all of the continuum states are taken into account in Eq. (35).

Figs. 5(a)–5(f), we clearly find gradual convergence into a pattern that is similar to the full result in Fig. 3(d). Hence, in order to reproduce the intensity dependence of R correctly, it is necessary to take into account a large number of bound states up to the Rydberg regime. In fact, the energies of the 20th and 30th excited states in the potential of Eq. (18) with $Z = 1.0$ are only -4.72×10^{-3} a.u. and -2.22×10^{-3} a.u., respectively. To see the asymmetry oscillation as a function of the pulse amplitude more clearly, Fig. 6 shows cuts of Fig. 5

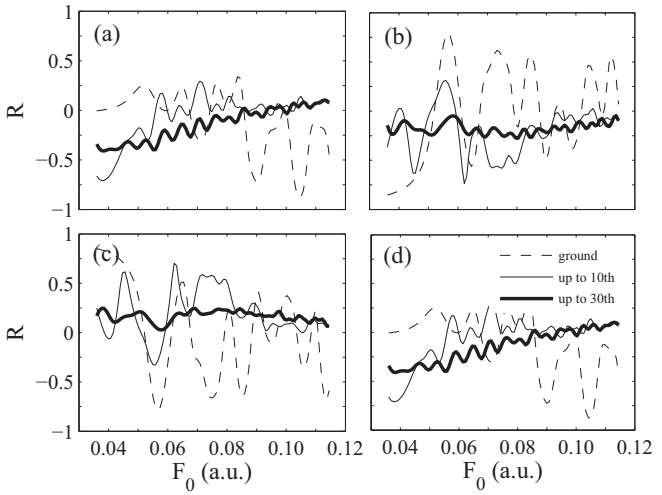

FIG. 6. Asymmetry of the photoelectron momentum distributions as a function of the field strength for a 1D model atom with the potential of Eq. (18) at a wavelength $\lambda = 800$ nm for some fixed values of CEP: (a) $\varphi = 0$, (b) $\varphi = \pi/2$, (c) $\varphi = 3\pi/2$, and (d) $\varphi = 2\pi$. The dashed, thin solid, and thick solid curves show cuts of Figs. 5(a), 5(d), and 5(f), respectively.

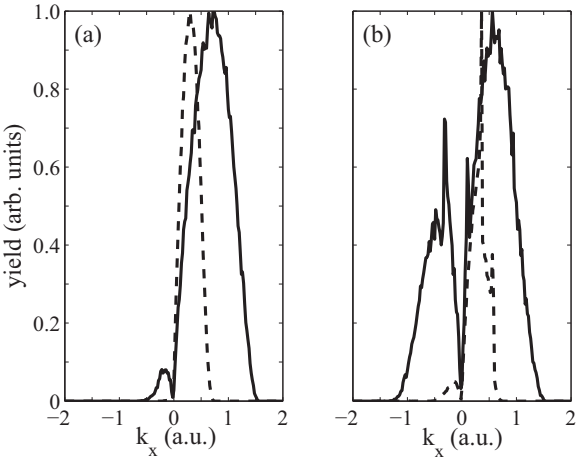

FIG. 7. Photoelectron momentum distributions calculated using the two-step model for ionization of a 1D model atom [Eq. (18)] by a pulse with a duration of (a) $n_p = 2$ and (b) $n_p = 4$. The dashed and solid curves correspond to $F_0 = 0.05$ a.u. and $F_0 = 0.09$ a.u., respectively. The wavelength is $\lambda = 800$ nm and the CEP is $\varphi = 1.38\pi$.

at some fixed values of the CEP: $\varphi = 0$, $\pi/2$, $3\pi/2$, and 2π. In conclusion, the oscillations of the asymmetry parameter as a function of the laser intensity are a result of a complex interference effect, in which both bound and continuum states are involved.

3. *Effect of the pulse length*

The disappearance of the asymmetry oscillations with decreased pulse duration [cf. Figs. 2(a) and 2(d)] can be understood on the basis of the two-step model with the Coulomb field. Momentum distributions calculated using the two-step semiclassical model are shown in Figs. 7(a) and 7(b) for two different pulse durations ($n_p = 2$ and 4) and field strengths ($F_0 = 0.05$ and 0.09 a.u.).

It is seen that at low intensity, the distributions consist of only one maximum (centered at some $k_x > 0$) for both pulse lengths. Moreover, in both cases, the second maximum of the distributions corresponding to $k_x < 0$ appears at higher intensities. However, its height and width are substantially different depending on the pulse duration: this second maximum is much smaller for the shorter pulse because of the more intensive population of the Rydberg states. Indeed, in accord with the scaling obtained in Ref. [51], the number of electrons captured into the Rydberg states after the end of the pulse increases with the decreasing pulse duration. As a result, even a substantial interference effect cannot lead to a significant change of the asymmetry of the photoelectron momentum distributions generated by such a short pulse, and the Coulomb attraction [28,29] is the only mechanism determining the asymmetry in this case.

IV. CONCLUSIONS

In conclusion, we have revisited the left-right asymmetry of the photoelectron momentum distributions generated by an intense few-cycle laser pulse in the subtunneling regime,

where $1 < \gamma < 2$. We have investigated the asymmetry as a function of both the absolute phase and laser intensity for the atomic hydrogen using *ab initio* numerical solution of the 3D TDSE, semiclassical simulations based on the two-step model accounting for both the laser field and the Coulomb field of the ion, and the SFA. We have shown that in the well-studied intensity region of $0.3–1.0 \times 10^{14}$ W/cm^2, the left-right asymmetry exhibits nontrivial behavior, which was discussed earlier in the case of ionization of a one-dimensional model atom [31]. In particular, our TDSE calculations demonstrate distinctive oscillations of the asymmetry parameter as a function of the intensity for a fixed CEP: at some laser intensities, the asymmetry turns to zero, i.e., photoelectron momentum distributions restore their symmetry. It is shown that these oscillations cannot be described within the SFA, which is in qualitative agreement with the conclusions of Refs. [27–29]. However, they also cannot be described by the semiclassical simulations, even when both laser field and the Coulomb potential of the ion are taken into account. This implies that the asymmetry in the subtunneling intensity regime appears not only due to the Coulomb attraction of an ionized electron.

In order to reveal the physical mechanism responsible for this intricate change of the asymmetry of momentum distributions, we have investigated the same effect in a one-dimensional model. Here we have applied the same methods, namely, TDSE (both in coordinate and momentum space), one-dimensional counterpart of the SFA, and semiclassical two-step model with both fields. By solving the momentum-space TDSE in a basis of eigenfunctions of binding potential, we have revealed the mechanism of the formation of the photoelectron momentum distributions and of their asymmetry. We have shown that the quantum interference of a large number of bound and continuum states underlies the oscillations of the left-right asymmetry with the intensity variation at a fixed CEP.

ACKNOWLEDGMENTS

We are grateful to Niels Carl Hansen (Aarhus University) for his valuable assistance in numerical solution of the 3D TDSE. This work was supported by the European Community's FP7 through the CRONOS Project No. 126205, the Danish Center for Scientific Computation, the Danish Natural Science Research Council, the ERC-StG (Project No. 277767-TDMET), the Academy of Finland, the NORDFORSK network "Time-domain quantum processes studied by ultrafast radiation pulses," and the COST Action Project No. CM1204 (XLIC-XUV/X-ray light and fast ions for ultrafast chemistry).

[1] F. Krauzs and M. Ivanov, Rev. Mod. Phys. **81**, 163 (2009).
[2] T. Brabec and F. Krausz, Rev. Mod. Phys. **72**, 545 (2000).
[3] G. G. Paulus, F. Grasbon, H. Walther, P. Villoresi, M. Nisoli, S. Stagira, E. Priori, and S. De Silvestri, Nature (London) **414**, 182 (2001).
[4] A. Baltuška, T. Udem, M. Uiberacker, M. Hentschel, E. Goulielmakis, C. Gohle, R. Holzwarth, V. S. Yakovlev, A. Scrinzi, T. W. Hänsch, and F. Krausz, Nature (London) **421**, 611 (2003).
[5] A. Baltuška, M. Uiberacker, E. Goulielmakis, R. Kienberger, V. S. Yakovlev, T. Udem, T. W. Hänsch, and F. Krausz, IEEE J. Sel. Top. Quantum Electron. **9**, 972 (2003).
[6] M. Kakehata, H. Takada, Y. Kobayashi, and K. Torizuka, Opt. Express **12**, 2070 (2004).
[7] K. O'Keeffe, P. Jöckl, H. Drexel, V. Grill, F. Krausz, and M. Lezius, Appl. Phys. B: Lasers Opt. **78**, 583 (2004).
[8] E. Gagnon, I. Thomann, A. Paul, A. Lytle, S. Backus, M. Murnane, H. Kapteyn, and A. Sandhu, Opt. Lett. **31**, 1866 (2006).
[9] K. H. Hong, J. Lee, B. Hou, J. A. Nees, E. Power, and G. A. Mourou, Appl. Phys. Lett. **89**, 031113 (2006).
[10] V. Roudnev and B. D. Esry, Phys. Rev. Lett. **99**, 220406 (2007).
[11] Christian Per Juul Martiny and L. B. Madsen, Phys. Rev. Lett. **97**, 093001 (2006).
[12] D. B. Milošević, G. G. Paulus, D. Bauer, and W. Becker, J. Phys. B **39**, R203 (2006).
[13] A. de Bohan, P. Antoine, D. B. Milošević, and B. Piraux, Phys. Rev. Lett. **81**, 1837 (1998).
[14] V. S. Yakovlev and A. Scrinzi, Phys. Rev. Lett. **91**, 153901 (2003).
[15] M. Nisoli, G. Sansone, S. Stagira, S. De Silvestri, C. Vozzi, M. Pascolini, L. Poletto, P. Villoresi, and G. Tondello, Phys. Rev. Lett. **91**, 213905 (2003).
[16] C. A. Haworth, L. E. Chipperfield, J. S. Robinson, P. L. Knight, J. P. Marangos, and J. W. G. Tisch, Nat. Phys. **3**, 52 (2007).
[17] A. D. Bandrauk, S. Chelkowski, D. J. Diestler, J. Manz, and K. J. Yuan, Phys. Rev. A **79**, 023403 (2009).
[18] P. Huang, X. T. Xie, X. Lü, J. Li, and X. Yang, Phys. Rev. A **79**, 043806 (2009).
[19] G. Sansone, E. Benedetti, J. P. Caumes, S. Stagira, C. Vozzi, M. Nisoli, L. Poletto, P. Villoresi, V. Strelkov, I. Sola, L. B. Elouga, A. Zaïr, E. Mével, and E. Constant, Phys. Rev. A **80**, 063837 (2009).
[20] X. Liu, H. Rottke, E. Eremina, W. Sandner, E. Goulielmakis, K. O. Keeffe, M. Lezius, F. Krausz, F. Lindner, M. G. Schätzel, G. G. Paulus, and H. Walther, Phys. Rev. Lett. **93**, 263001 (2004).
[21] X. Liu and C. Figueira de Morisson Faria, Phys. Rev. Lett. **92**, 133006 (2004).
[22] G. G. Xin, D. F. Ye, and J. Liu, Phys. Rev. A **82**, 063423 (2010).
[23] T. Shaaran, C. Figueira de Morisson Faria, and H. Schomerus, Phys. Rev. A **85**, 023423 (2012).
[24] N. I. Shvetsov-Shilovski, A. M. Sayler, T. Rathje, and G. G. Paulus, Phys. Rev. A **83**, 033401 (2011).
[25] N. I. Shvetsov-Shilovski, A. M. Sayler, T. Rathje, and G. G. Paulus, New J. Phys. **13**, 123015 (2011).
[26] M. F. Kling, Ch. Siedschlag, A. J. Verhoef, J. I. Khan, M. Schultze, Th. Uphues, Y. Ni, M. Uiberacker, M. Drescher, F. Krausz, and M. J. J. Vrakking, Science **312**, 246 (2006).

[27] S. Chelkowski and A. D. Bandrauk, Phys. Rev. A **65**, 061802 (2002).
[28] S. Chelkowski, A. D. Bandrauk, and A. Apolonski, Phys. Rev. A **70**, 013815 (2004).
[29] S. Chelkowski and A. D. Bandrauk, Phys. Rev. A **71**, 053815 (2005).
[30] L. V. Keldysh, Zh. Eksp. Teor. Fiz. **47**, 1945 (1964) [Sov. Phys. JETP **20**, 1307 (1965)].
[31] G. G. Paulus in *Progress in Ultrafast Intense Laser Science IV*, edited by K. Yamanouchi, A. Becker, R. Li, and S. L. Chin (Springer, Berlin, 2009).
[32] F. H. M. Faisal, J. Phys. B **6**, L89 (1973).
[33] H. R. Reiss, Phys. Rev. A **22**, 1786 (1980).
[34] H. B. van Linden van den Heuvell and H. G. Muller, in *Multiphoton Processes*, edited by S. J. Smith and P. L. Knight (Cambridge University Press, Cambridge, U.K., 1988).
[35] T. F. Gallagher, Phys. Rev. Lett. **61**, 2304 (1988).
[36] T. K. Kjeldsen, L. A. A. Nikolopoulos, and L. B. Madsen, Phys. Rev. A **75**, 063427 (2007).
[37] T. K. Kjeldsen, Ph.D. thesis, University of Århus, Århus, Denmark, 2007.
[38] C. P. J. Martiny, M. Abu-samha, and L. B. Madsen, Phys. Rev. A **81**, 063418 (2010).
[39] N. I. Shvetsov-Shilovski, D. Dimitrovski, and L. B. Madsen, Phys. Rev. A **85**, 023428 (2012).
[40] N. I. Shvetsov-Shilovski, D. Dimitrovski, and L. B. Madsen, Phys. Rev. A **87**, 013427 (2013).
[41] L. D. Landau and E. M. Lifschitz, *Quantum Mechanics Nonrelativistic Theory*, 2nd ed. (Pergamon, Oxford, 1965).
[42] D. Dimitrovski, C. P. J. Martiny, and L. B. Madsen, Phys. Rev. A **82**, 053404 (2010).
[43] A. N. Pfeiffer, C. Cirelli, M. Smolarski, D. Dimitrovski, M. Abu-Samha, L. B. Madsen, and U. Keller, Nat. Phys. **8**, 76 (2012).
[44] J. Maurer, D. Dimitrovski, L. Christensen, L. B. Madsen, and H. Stapelfeldt, Phys. Rev. Lett. **109**, 123001 (2012).
[45] T. Brabec, M. Côte, P. Boulanger, and L. Ramunno, Phys. Rev. Lett. **95**, 073001 (2005).
[46] A. M. Perelomov, V. S. Popov, and M. V. Terent'ev, Zh. Eksp. Teor. Fiz. **50**, 1393 (1966) [Sov. Phys. JETP **23**, 924 (1966)].
[47] M. V. Ammosov, N. B. Delone, and V. P. Krainov, Zh. Eksp. Teor. Fiz. **91**, 2008 (1986) [Sov. Phys. JETP **64**, 1191 (1986)].
[48] N. B. Delone and V. P. Krainov, J. Opt. Soc. Am. B **8**, 1207 (1991).
[49] W. H. Press, S. A. Teukolsky, W. T. Vetterling, and B. P. Flannery, *Numerical Recipes in Fortran 77: The Art of Scientific Computing*, 2nd ed. (Cambridge University Press, Cambridge, U.K., 1992).
[50] T. Nubbemeyer, K. Gorling, A. Saenz, U. Eichmann, and W. Sandner, Phys. Rev. Lett. **101**, 233001 (2008).
[51] N. I. Shvetsov-Shilovski, S. P. Goreslavski, S. V. Popruzhenko, and W. Becker, Laser Phys. **19**, 1550 (2009).
[52] G. F. Gribakin and M. Yu. Kuchiev, Phys. Rev. A **55**, 3760 (1997).
[53] S. F. C. Shearer, M. C. Smyth, and G. F. Gribakin, Phys. Rev. A **84**, 033409 (2011).
[54] E. Cormier and P. Lambropoulos, Eur. Phys. J. D **2**, 15 (1998).
[55] M. G. Makris and P. Lambropoulos, J. Phys. B **37**, 2247 (2004).
[56] J. Javanainen, J. H. Eberly, and Q. Su, Phys. Rev. A **38**, 3430 (1988).
[57] W. G. Greenwood and J. H. Eberly, Phys. Rev. A **43**, 525 (1991).
[58] L. B. Madsen, L. A. A. Nikolopoulos, T. K. Kjeldsen, and J. Fernández, Phys. Rev. A **76**, 063407 (2007).
[59] G. A. Evans, Appl. Numer. Math. **14**, 383 (1994).
[60] G. A. Evans, Int. J. Comput. Math. **52**, 185 (1994).
[61] L. N. G. Filon, Proc. R. Soc. Edinburgh **49**, 38 (1928).